

Single source CARS-based multimodal microscopy system for biological tissue imaging [Invited]

MINGYU SHENG,^{1,†} YUAN ZHAO,^{1,†} ZHENGUO WU,^{1,2} JIANHUA ZHAO,^{1,2} HARVEY LUI,^{1,2}  SUNIL KALIA,^{2,3,4,5} AND HAISHAN ZENG^{1,2,*} 

¹Imaging Unit - Integrative Oncology Department, BC Cancer Research Institute, 675 West 10th Avenue, Vancouver, BC, V5Z 1L3, Canada

²Photomedicine Institute, Department of Dermatology and Skin Science, University of British Columbia and Vancouver Coastal Health Research Institute, Vancouver, Canada

³Department of Cancer Control Research, BC Cancer Research Institute, Vancouver, Canada

⁴BC Children's Hospital Research Institute, Vancouver, Canada

⁵Centre for Clinical Epidemiology and Evaluation, Vancouver Coastal Health Research Institute, Vancouver, Canada

[†]These two authors contributed equally to the manuscript.

*hzeng@bccrc.ca

Abstract: A coherent anti-Stokes Raman scattering (CARS)-based multimodality microscopy system was developed using a single Ti:sapphire femtosecond laser source for biological imaging. It provides three complementary and co-registered imaging modalities: CARS, MPM (multiphoton microscopy), and RCM (reflectance confocal microscopy). The imaging speed is about 1 frame-per-second (fps) with a digital resolution of 1024×1024 pixels. This microscopy system can provide clear 2-dimensional and 3-dimensional images of *ex-vivo* biological tissue samples. Its spectral selection initiates vibrational excitation in lipid cells (approximately 2850 cm^{-1}) using two filters on the pump and Stokes beam paths. The excitation can be tuned over a wide spectral range with adjustable spectral filters. The imaging capability of this CARS-based multimodal microscopy system was demonstrated using porcine fat, murine skin, and murine liver tissue samples.

© 2023 Optica Publishing Group under the terms of the [Optica Open Access Publishing Agreement](#)

1. Introduction

In the past few decades, the progress in the field of optical microscopy has been revolutionary. Various multimodal laser-scanning microscopies have emerged. Multimodal laser-scanning microscopy is created by integrating multiple imaging modalities into a single system [1–4]. Multimodal microscopy uses two or more complementary contrast mechanisms to form 3D volumetric images of tissues. The imaging mechanisms include confocal, two-photon excitation fluorescence (TPEF) [5–10], second harmonic generation (SHG) [11–15], third harmonic generation (THG) [16–19], and coherent anti-Stokes Raman scattering (CARS) [20–24]. Each of these mechanisms has an inherent optical slicing capability. These techniques can be applied to unlabeled samples to visualize molecular and morphological structures that are previously invisible. Because each module can detect specific molecules or structures, multimodal laser-scanning microscopy enables the study of complex biological tissues, biological processes, lipid metabolism, and facilitates cancer detection and diagnosis.

Even though many multimodal systems have been developed in the past, including systems with CARS and MPM technology, no existing multimodal systems combine CARS, MPM and RCM (reflectance confocal microscopy). Including RCM [25–32] into the multimodal system can simultaneously provide overall information about chemical and morphological characteristics of

biological tissue [28]. RCM imaging is currently being used for improving diagnostic accuracy and early detection of skin cancer [29]. It has also been found to accurately depict the lateral tumor edges of these cancers [28,29], allowing for instantaneous confirmation of tumor margin clearance during surgery. Because of all the benefits and advantages of the RCM technology, we decided to incorporate it into our CARS based multimodal microscopy system.

Furthermore, the existing single-source CARS-based multimodal system is attractive for its simplicity and quick implementation [33]. We developed a multimodal microscopy system by adding RCM into the CARS system. It employs a single-laser source and one objective lens. The single femtosecond pulsed laser source emits signals with a wide wavelength range. The system provides three unique microscopy techniques (RCM, MPM and CARS) to offer subcellular-spatial-resolution imaging on unlabeled tissue samples. The three imaging signals were measured simultaneously by three detectors with three specific filters in the front. The system has improved sensitivity and achieved high signal-to-noise ratio. The detector in the CARS channel works in the photon counting mode. It achieved a frame rate of 1fps, which offers a more complete and enhanced visual contrast of the samples. Imaging of collagen, elastin, and lipid rich regions in biological tissue samples were demonstrated

2. Materials and methods

2.1. Tissue sample preparation

The tissue samples were prepared under experimental protocols approved by the University of British Columbia's Animal Care Committee (certificate number: A18-0035). Three types of biological tissue were used in this research: porcine adipose tissue, murine ear, and murine liver. These biological tissue samples were fixed in formalin before measurement.

2.2. Experimental setup of CARS-based multimodal microscopy

The experimental setup is schematically shown below in Fig. 1. The light source was a 90 MHz Ti: Sapphire femtosecond laser (Chameleon, Coherent Inc., Santa Clara, California). The output beam was tuned to 808 nm. To prevent any reflected light from returning to the femtosecond laser oscillator cavity, a Faraday isolator (F1) was placed in front of the laser. The beam from the laser source entered the Faraday isolator and was then divided into two arms by a 50/50 ultrafast beam splitter (BS) to form the pump and Stokes beams. The intensity of each beam was decreased to avoid damage of the tissue sample with two separate attenuators (attenuator 1 and attenuator 2). These attenuators consisted of a half wave plate (Newport 10RP52-2) and a Glan-Laser Calcite Polarizer (Newport, 10GL08AR). The Stokes beam was then passed through a Newport supercontinuum generation kit (SCG-800) to generate a supercontinuum light beam covering the spectral range of 400 nm - 2000nm. In order to generate the CARS signal, both beams must be matched in their optical pathlengths. Thus each beam was paired with its own delay line to allow adjustments to create the CARS signal. Following each delay line, a bandpass filter was used to filter the optical spectrum. BP1 (1050-50 OD4 bandpass filter, Alluxa) was used to narrow the Stokes beam bandwidth to 50 nm with a central wavelength of 1050 nm, while a BP2 (LL01-808-25, Semrock) was used to narrow the pump beam bandwidth to 3 nm with a central wavelength of 808 nm. The optical power at the sample was ~12 mW for the pumping beam and ~1.5 mW for the Stokes beam. This pump/Stokes combination facilitated CARS imaging of lipid Raman band around 2852 cm^{-1} .

After the beams were adjusted to match each other in the optical pathlengths, the two beams were then combined using an 808 nm RELP long pass filter (RELP). For two-dimensional scanning, the combined collimated beam passed through a pair of galvano mirrors (GM: GVS002, Thorlabs). The scanner had a field of view of $200 \times 200\text{ }\mu\text{m}$ and an imaging resolution of 1024×1024 pixels. Following the scanner, a beam expander was used to expand the beam and

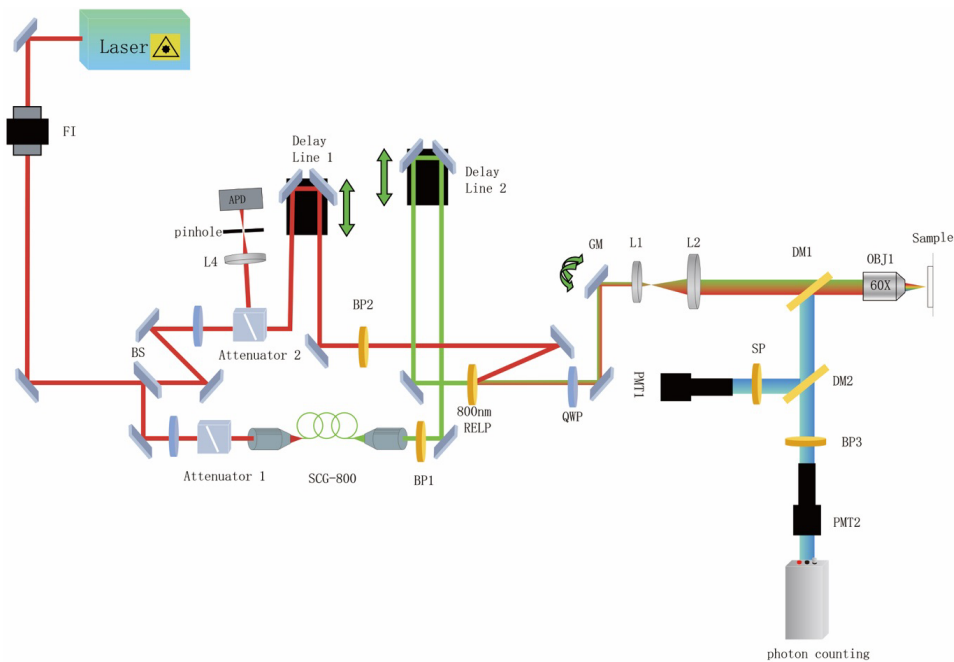


Fig. 1. Block diagram of CARS-based multimodal microscopy system using a single laser source and a single objective lens. FI (Faraday isolator), BS (beam splitter), Attenuator (a half wave plate and a Glan-Laser Calcite Polarizer), SCG-800 (supercontinuum generation kit), RELP (razor edge long pass filter), LP (long pass filter), OBJ (objective lens), SP (short pass filters), BP (band pass filters), DM (dichroic mirror), L (Lens), and PMT (photomultiplier). APD: avalanche photodiode.

provided a uniform imaging performance across the entire rear aperture of the objective lens (LUMPLFLN60XW, Olympus). This beam expander had a dual-telecentric configuration with 2.0 \times magnification; it consisted of two achromatic doublets, specifically a scan lens (AC254-050-B, Thorlabs) and a tube lens (AC254-100-B, Thorlabs). Following the beam expander, the overlapped and collimated Stokes and pump beam were focused using an objective lens onto the sample to generate CARS, MPM and RCM signals. The sample was placed on a motorized translational stages, which with the use of a pair of galvano mirrors was able to enable the multimodal system to produce 3D images.

For multimodal image acquisition, our system employed both the descanned and non-descanned detection schemes. The non-descanned detection configuration was used for MPM and CARS signal acquisition, while the descanned detection configuration was used for RCM signal acquisition. In order to detect three signals simultaneously, dichroic mirrors were used to separate them from each other. RCM signal was the first to be separated from the combined signals, using a dichroic mirror (DM1: FF665-Di02-2536, Semrock) with a cut-off wavelength of 665 nm. The dichroic mirror DM1 transmitted the RCM signal and reflected both the MPM and the CARS signals. Following this, the CARS signal was then separated from the MPM signal using another dichroic mirror (DM2: FF605-Di02-25 \times 36, Semrock) with a cut-off wavelength of 605 nm. The DM2 transmitted the CARS signal and reflected the MPM signal. Before the MPM and CARS signals were measured by their respective detectors, two emission filters were used to reduce background noise. For the CARS signal channel, a 650 nm bandpass filter (FF02-655/40-25, Semrock, bandwidth = 40 nm) was employed, and for the MPM signal channels, a 650 short-pass filter (FF01-650/SP-25, Semrock, passing light between 350–650 nm) was used. This facilitated

collection of the integrated TPEF and SHG signals generated by both the pump beam and the Stokes beam. This integration design assured the MPM channel having good signal-to-noise ratio, considering the excitation optical power used in the CARS channel (13.5 mW), which is also the MPM excitation power in our system, is considerably lower than that of conventional MPM system (30–60 mW).

Two types of detectors were used in this system. The CARS signal was detected using a photomultiplier tube (PMT) working in a photon counting mode (R3896, C12597-04, C9744, Hamamatsu). The MPM signal was also detected using a photomultiplier tube PMT1 (R3896, Hamamatsu), but in analog mode. Working in a descanned mode, RCM signal was detected by an avalanche photodiode APD (C10508-01, Hamamatsu) after passing through the beam expander, scanning device, RELP, delay line, and a pinhole (150 μm). To reduce scattered light from optical elements, a quarter wave plate (QWP, wpq20me-780, Thorlabs) was used. The APD and the pinhole for RCM detection is located after the signal has passed through the scanner to become descanned signal. And they are located after the attenuator 2 to utilize the reflective polarizer within it to realize the RCM signal detection without using another polarizer, which will otherwise affect the pump beam transmission. Although the optical components in between will attenuate the RCM signal, we still get good enough signal-to-noise ratio RCM images because the RCM signal is quite strong.

3. Experimental results

3.1. 2D and 3D CARS imaging of biological tissue

The imaging capabilities of the CARS module were first demonstrated using unlabeled samples. The resulting images demonstrated that the CARS module was able to provide *ex vivo* imaging with subcellular spatial resolution. Figure 2. shows an *ex vivo* CARS image using porcine adipose tissue. Abundant lipid cells from the tissue sample were captured. The presence of rich lipid in the intracellular mortar generated high CARS signals and enabled brilliant polygonal cuticles to be clearly visible.

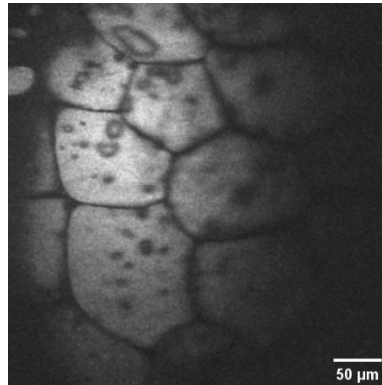


Fig. 2. CARS image of *ex vivo* porcine adipose tissue with field of view of 400 μm (FOV = 400 μm).

The cellular structures of a murine ear was measured using the CARS module. The sebaceous glands, shown in Fig. 3(a), were filled with micron-sized sebum particles - a compound rich in triglycerides and wax esters. Figure 3(b) depicts the subcutaneous fat layer, which was located at the bottom of the dermis in the murine skin.

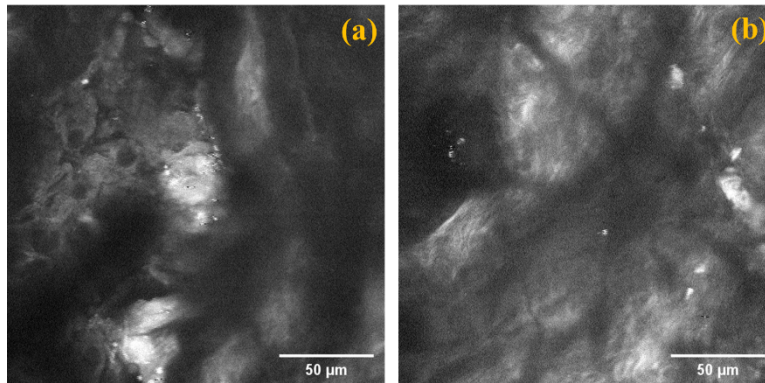


Fig. 3. CARS imaging of *ex vivo* murine ear skin with field of view of 200 μm (FOV = 200 μm). (a) sebaceous gland (b) subcutaneous fat layer.

The CARS microscope module was used to visualize murine liver tissues, see Fig. 4. Images 4(a) and 4(b) were captured at the same depth but at different locations. The liver tissue contained well distributed hepatic lipids that allows for strong CARS signals.

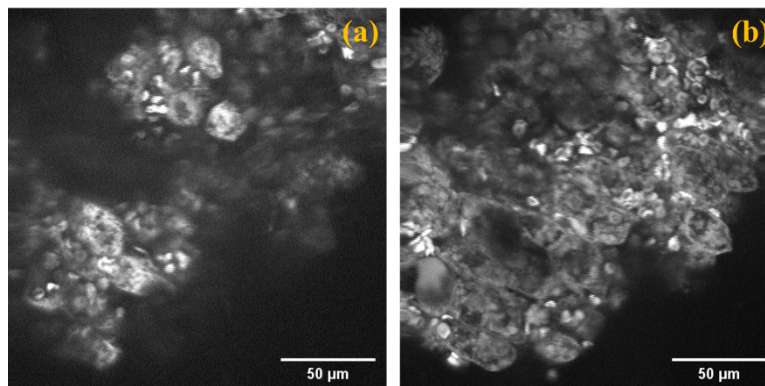


Fig. 4. CARS imaging of *ex vivo* murine liver with field of view at the same depth but at different locations (FOV = 200 μm).

CARS microscope module could also be used to create 3D volumetric images by using a motorized translational stage and a two-dimensional scanning unit - a pair of galvano mirrors. A video of a 2 mm thick liver tissue recorded through the CARS channel is shown in Fig. 5 (a). The intensity of the CARS signal was first increased with depth because the distribution of lipid cells was denser with the increase of scanning depth. Subsequently, the CARS signal was attenuated due to scattering and absorption until the signal almost disappeared at a depth of 40 μm . Figure 5(b) features a volumetric 3D CARS image composed of a series of 2D images. This 3D image was post-processed by stacking a series of 2D images using ImageJ, resulting in a 3D image of 200 μm x 200 μm x 40 μm in X, Y, and Z directions. The image can be rotationally visualized in 3D with a 3D viewer plugin, which provides more detailed information about the overall distribution of lipid droplets within the tissue sample.

3.2. Multimodal microscopy imaging of biological tissues

The multimodal microscope was capable of simultaneously imaging unlabeled, bulk samples using three different modules: MPM, CARS and RCM, which provided distinct and unique

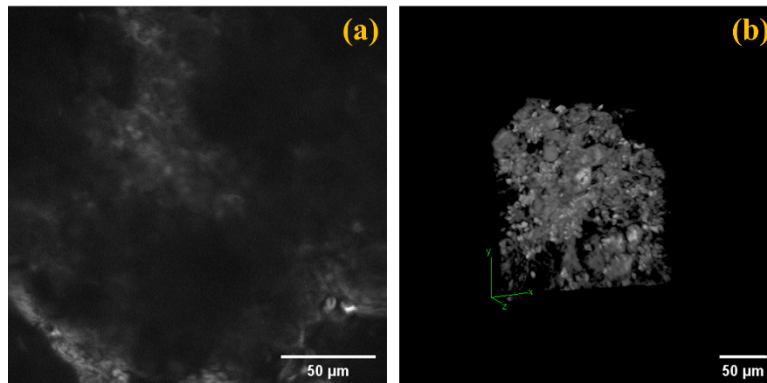


Fig. 5. (a) CARS video of a murine liver tissue (FOV = 200 μm), see [Visualization 1](#) for playing the video; (b) Volumetric CARS 3D image of a murine liver tissue at depth 40 μm (FOV = 200 μm), see [Visualization 2](#).

information individually to offer new insights and comprehensive understanding of biological tissues. Imaging of murine ear and liver tissue samples using the multimodal microscopic system is shown in Fig. 6 and Fig. 7.

Figure 6 shows the multimodal images of the murine ear skin. Figure 6(a) is the CARS image, showing the shape and distribution of lipids cells in the murine ear skin sample. Figure 6(b) is the RCM image displaying the scattering structures of the murine skin. Figure 6(c) is the MPM image, showing the distribution of endogenous fluorophores and SHG molecules, such as NADH, elastin, collagen, and fibroblasts. Figure 6(d) shows the two-color composite image that combined the CARS and RCM channels (green: CARS; red: RCM). In this particular two-color scheme, a pixel or region with green color means that the CARS signals dominate; red color means RCM signals dominate; while yellow color means there are both CARS signals and RCM signals originated from the same pixel or region. The distribution and interrelationship of different components of the murine ear skin is clearly seen from this composite image. We see both red color dominated regions and green color dominated regions, suggesting that CARS and RCM provide complimentary information. Figure 6(e) shows the two-color composite image that combined the CARS and the MPM channels (green: CARS; red: MPM). We see most regions with dominating green color (CARS dominant) and two large yellow clusters, suggesting comparable CARS and MPM contributions.

Figure 7 shows the multimodal images of a murine liver sample: CARS image (a), RCM image (b), MPM image (c), as well as two-color composite image (d) (green: CARS, red: RCM) and (e) (green: CARS, red: MPM). Similar to Fig. 6, Fig. 7(a) shows the shape and distribution of lipids cells in the murine liver. Figure 7 (b) displays the scattering structures of the murine liver. Figure 7 (c) shows the distribution of endogenous fluorophores and SHG molecules in the murine liver. And Fig. 7 (d) shows the two-color composite image that combined the CARS and RCM channels (green: CARS; red: RCM). The distribution and interrelationship of different components of the murine liver is clearly seen from this composite image. We see both red color dominated regions and green color dominated regions, suggesting that CARS and RCM provide complimentary information. There are also some yellow structures, suggesting considerable contributions of both CARS and MPM. Figure 7(e) shows the two-color composite image that combined the CARS and the MPM channels (green: CARS; red: MPM). We see most regions with dominating green color (CARS dominant) and quite some yellow clusters, suggesting comparable CARS and MPM contributions.

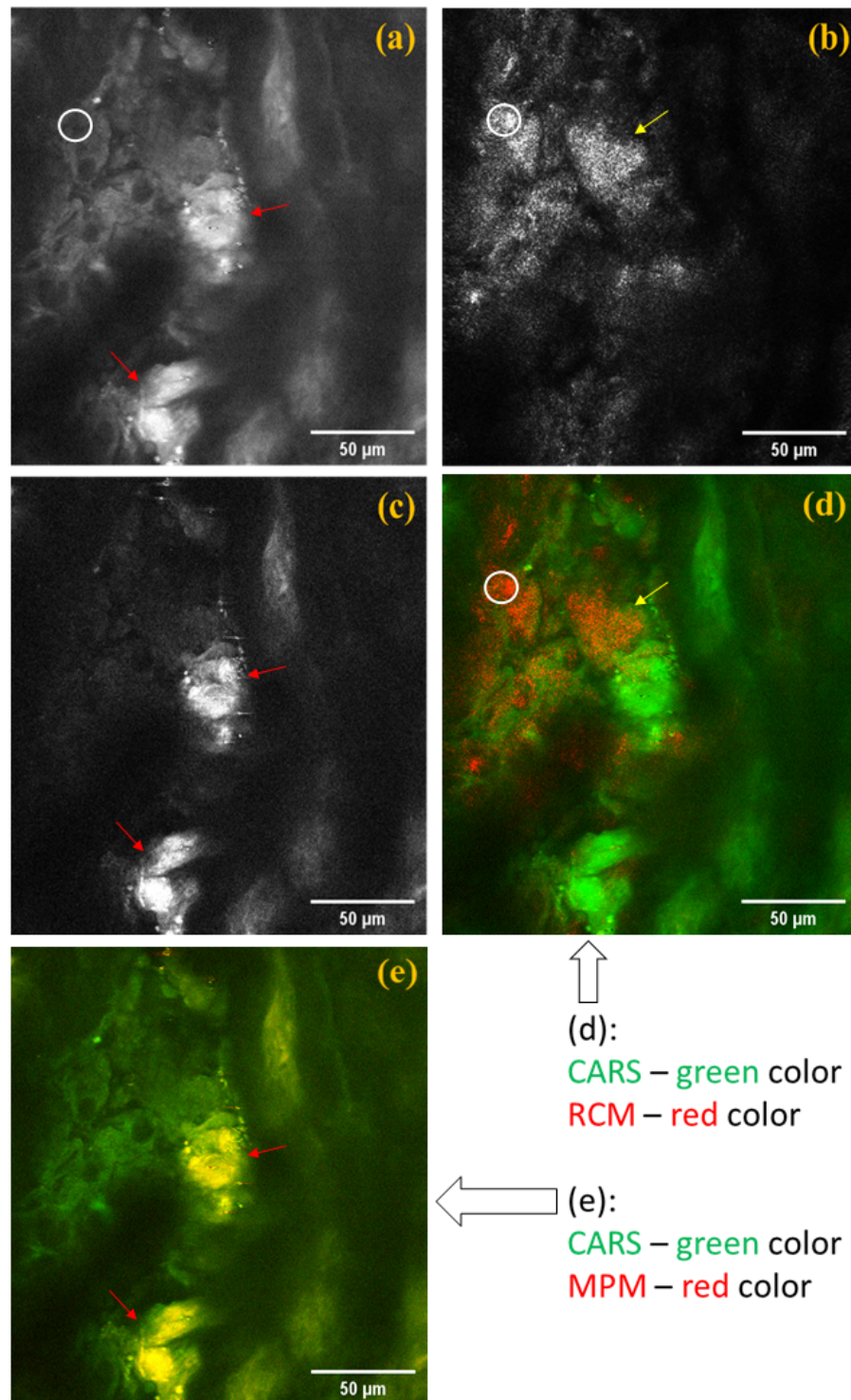


Fig. 6. Multimodal microscopic images of a murine ear tissue sample (FOV = 200 μm) (a) CARS image; (b) RCM image; (c) MPM image; (d) two-color composite image of CARS and RCM (green: CARS, red: RCM); (e) two-color composite image of CARS and MPM (green: CARS, red: MPM).

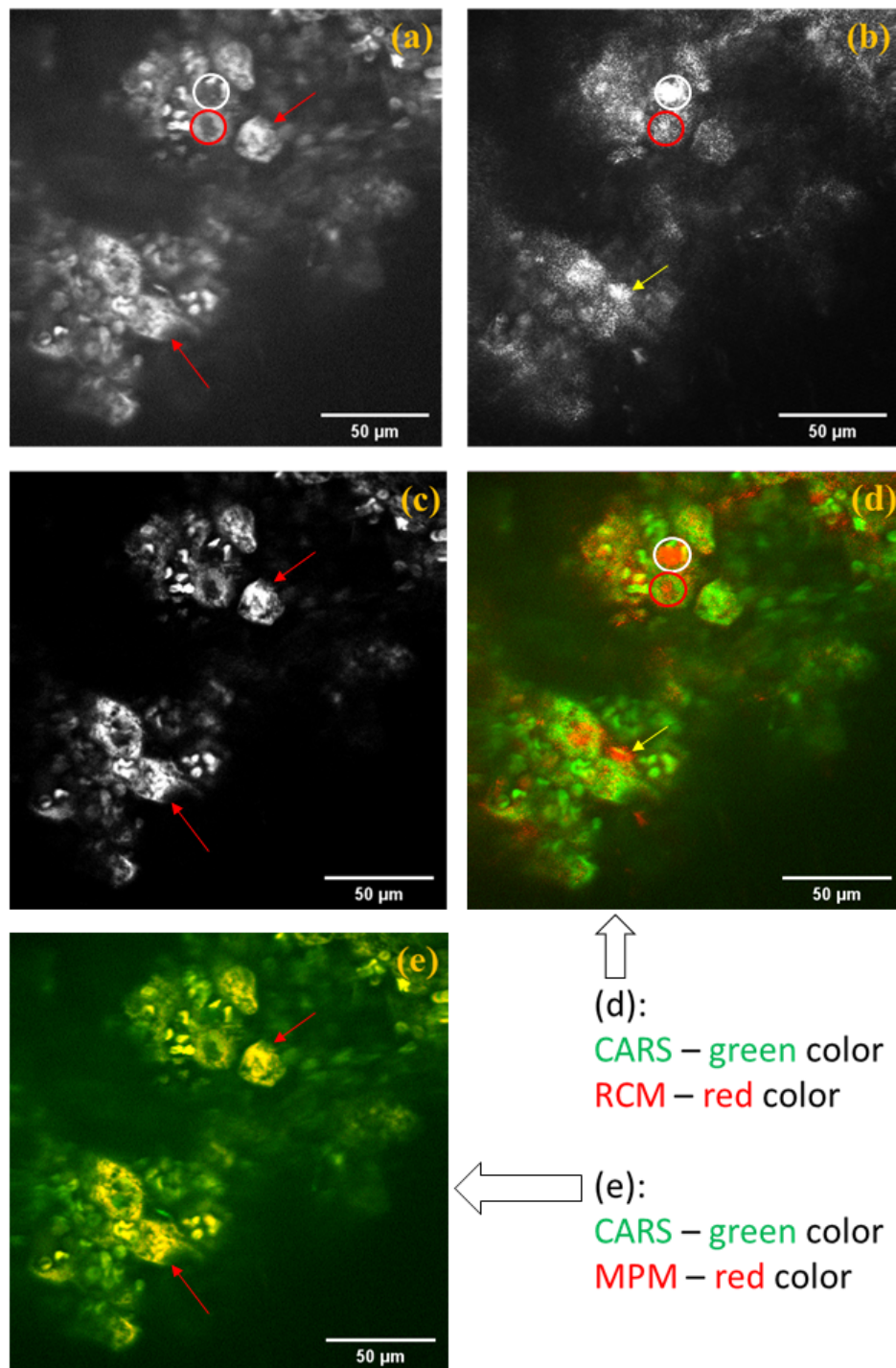


Fig. 7. Multimodal microscopic images of a murine liver sample (FOV = 200 μm) (a) CARS image; (b) RCM image; (c) MPM image; (d) two-color composite image of CARS and RCM (green: CARS, red: RCM); (e) two-color composite image of CARS and MPM (green: CARS, red: MPM).

4. Discussions and conclusions

We developed a CARS-based multimodal microscopy system that specifically combined RCM, MPM and CARS technology to simultaneously produce co-registered images of an unlabeled bulk tissue sample in the same region of interest, with subcellular resolution and high signal-to-noise ratio. The imaging speed was about 1 fps with a digital resolution of 1024×1024 pixels. The system had been tested experimentally using animal tissue samples. The results showed that different imaging modalities provide complimentary information about tissue chemistry and structures. CARS is well known for providing specific chemical component imaging. In this study, the chosen chemical component is lipids, so we obtained excellent signal-to-noise ratio images from lipid rich tissue samples: porcine fat, murine ear skin, and murine liver. RCM images tissue scattering properties and is sensitive to refractive index fluctuations in tissue. MPM images the distribution of endogenous fluorophores and SHG molecules, such as NADH, elastin, collagen, and fibroblasts. We used two-color composite image display to visualize the complimentary nature of different imaging modalities. For example, the two-color composite image of CARS (green color coded) and RCM (red color coded) is shown in Fig. 6(d). Within the white circle, the bright red colored cluster suggests that there is a microstructure scattering light strongly. There is no CARS signal from this cluster (no green components within this circle and it is dark at this area in Fig. 6(a) as well), suggesting that this cluster/microstructure contains no lipids. The yellow arrow points to a large triangle structure with strong light scattering (with bright red color coded RCM signals). And the CARS image – Fig. 6(a) suggests that there is minimal lipids contents within this triangle area. Interestingly, in the two-color composite image of CARS (green) and MPM (red), as shown in Fig. 6(e), we found two big clusters with bright yellow color (pointed to by red arrows). This means that these two particular microstructures/clusters have both strong CARS signal (contains lipids) and strong MPM signals (contains fluorophores and/or SHG molecules). This is a very unique property. Most other areas in this composite image are pure green color, meaning there are plenty of lipids around most of these places.

Similarly, in Fig. 7(d), we observed clusters/microstructures (within the white circle and red circle, or pointed by the yellow arrows) showing strong RCM signals (strong light scattering), but no CARS signals (no lipids). In the two-color composite image of CARS (green) and MPM (red), as shown in Fig. 7(e), we found clusters with bright yellow color (pointed to by red arrows). This means that these particular microstructures/clusters have both strong CARS signal (contains lipids) and strong MPM signals (contains fluorophores and/or SHG molecules). Again this is a very unique property. All these unique structures as highlighted by circles and arrows in Fig. 6 and Fig. 7 deserve further detailed studies, including histology correlations.

This single-source multimodal microscopy system has three distinctive characteristics. Firstly, it uniquely combined RCM, MPM and CARS in a multimodal system using a single femtosecond pulsed laser and a single microscopic objective lens. This system is the first of its kind with the incorporation of RCM technology into a CARS system. With the addition of RCM, this system will become a highly effective and powerful multimodal microscopy tool for biology study and clinical diagnosis. This design also allowed imaging with ease of operation and simultaneous capture from the same region of interest. The using of a single source laser and simultaneous acquisition of all modes of images guaranteed the co-registration of all images. As we have demonstrated, adding RCM to a CARS system is quite straight forward. It can be easily implemented in any CARS system and greatly enhance its imaging capabilities. Secondly, the microscopic system used different detectors or detection mode for each channel: RCM was detected using an APD detector because it worked in a descanned mode; MPM was detected using a PMT detector working in an analog mode, and CARS was detected using a PMT working in a photon counting mode. With different detectors or detection mode, we achieved an overall higher imaging sensitivity and a higher signal-to-noise ratio. Thirdly, the system provided 2D

and 3D imaging capabilities because it was equipped with a 2D scanning unit that could conduct scans in the X and Y axis, and a motorized translational stage for Z axis imaging.

This multimodal system could be further improved in the future. The imaging speed of the current system was limited by its scanner speed. Currently it uses a 1 kHz Galvo scanner. The imaging speed could be further improved by using a faster scanner, such as an 8 or 16 kHz resonance scanner. The imaging speed could be improved by 8 or 16 times, enabling imaging capabilities for *in vivo* applications. Another improvement would be the ability to detect various chemical components in addition to lipids. Currently, the system used a band pass filter to select a narrow spectrum range from the Stokes beam within the broad waveband of 400 - 2000nm, which was effective for imaging lipids. The chemical component to be imaged is determined by the spectral range of the filter for the Stokes beam. If other bandpass filters are incorporated into the system, a wider range of chemical components could be imaged using this system.

In conclusion, we have developed a CARS-based multimodal microscopy system using a single femtosecond laser source and a single objective lens, which enabled co-registered imaging of CARS, MPM and RCM simultaneously. It provided faster imaging speed and had the capability to capture unique structures and chemical components of biological tissues. With further improvement, it would allow for monitoring more than one biological component and potentially be used for *in vivo* applications. We believe that our current development with future improvement of the CARS-based multimodal microscope will help improve biological research and medical diagnosis.

Funding. Canadian Institutes of Health Research (MOP130548); Canadian Dermatology Foundation; BC Hydro Employees Community Services Fund; VGH and UBC Hospital Foundation.

Disclosures. The authors declare no conflicts of interest.

Data availability. The authors confirm that the data supporting the findings of this study are either available within the article or could be obtained from the authors upon reasonable request.

References

1. S. H. Yue, M. N. Slipchenko, and J. X. Cheng, "Multimodal nonlinear optical microscopy," *Laser Photonics Rev.* **5**(4), 496–512 (2011).
2. E. C. Yang, I. S. Vohra, H. Badaoui, *et al.*, "Development of an integrated multimodal optical imaging system with real-time image analysis for the evaluation of oral premalignant lesions," *J. Biomed. Opt.* **24**(02), 1–10 (2019).
3. J. Ryu, U. Kang, J. W. Song, *et al.*, "Multimodal microscopy for the simultaneous visualization of five different imaging modalities using a single light source," *Biomed. Opt. Express* **12**(9), 5452–5469 (2021).
4. S. Pelicci, L. Furia, P. G. Pelicci, *et al.*, "Correlative multi-modal microscopy: a novel pipeline for optimizing fluorescence microscopy resolutions in biological applications," *Cells* **12**(3), 354 (2023).
5. W. Kaiser and C. G. B. Garrett, "Two-photon excitation in $\text{CaF}_2:\text{Eu}^{2+}$," *Phys. Rev. Lett.* **7**(6), 229–231 (1961).
6. W. Denk, J. H. Strickler, and W. W. Webb, "Two-photon laser scanning fluorescence microscopy," *Science* **248**(4951), 73–76 (1990).
7. D. W. Piston, "Imaging living cells and tissues by two-photon excitation microscopy," *Trends Cell Biol.* **9**(2), 66–69 (1999).
8. M. B. Ericson, C. Simonsson, S. Guldbrand, *et al.*, "Two-photon laser-scanning fluorescence microscopy applied for studies of human skin," *J. Biophotonics* **1**(4), 320–330 (2008).
9. R. K. P. Benninger and D. W. Piston, "Two-photon excitation microscopy for the study of living cells and tissues," *Curr. Protoc. Cell Biol.* **59**(1), 4.11.1 (2013).
10. K. Otomo, H. Ishii, and T. Nemoto, "Improving two-photon excitation microscopy for sharper and faster biological imaging," *Biophys. Physicobiol.* **20**(1), e200009 (2023).
11. S. Fine and W. P. Hansen, "Optical second harmonic generation in biological systems," *Appl. Opt.* **10**(10), 2350–2353 (1971).
12. Y. Guo, P. P. Ho, H. Savage, *et al.*, "Second harmonic tomography of tissues," *Opt. Lett.* **22**(17), 1323–1325 (1997).
13. I. Freund and M. Deutsch, "Second-harmonic microscopy of biological tissue," *Opt. Lett.* **11**(2), 94–96 (1986).
14. P. J. Campagnola, M. Wei, A. Lewis, *et al.*, "High-resolution nonlinear optical imaging of live cells by second harmonic generation," *Biophys. J.* **77**(6), 3341–3349 (1999).
15. X. Chen, O. Nadiarynkh, S. Plotnikov, *et al.*, "Second harmonic generation microscopy for quantitative analysis of collagen fibrillar structure," *Nat. Protoc.* **7**(4), 654–669 (2012).
16. D. Yelin and Y. Silberberg, "Laser scanning third-harmonic-generation microscopy in biology," *Opt. Express* **5**(8), 169–175 (1999).

17. N. V. Kuzmin, P. Wesseling, P. C. de Witt Hamer, *et al.*, "Third harmonic generation imaging for fast, label-free pathology of human brain tumors," *Biomed. Opt. Express* **7**(5), 1889–1904 (2016).
18. S. J. Ahn, N. E. Ruiz-Urbe, B. Li, *et al.*, "Label-free assessment of hemodynamics in individual cortical brain vessels using third harmonic generation microscopy," *Biomed. Opt. Express* **11**(5), 2665–2678 (2020).
19. M. Yildirim, M. Hu, N. M. Le, *et al.*, "Quantitative third-harmonic generation imaging of mouse visual cortex areas reveals correlations between functional maps and structural substrates," *Biomed. Opt. Express* **11**(10), 5650–5673 (2020).
20. R. F. Begley, A. B. Harvey, and R. L. Byer, "Coherent anti-Stokes Raman spectroscopy," *Appl. Phys. Lett.* **25**(7), 387–390 (1974).
21. A. Zumbusch, G. R. Holtom, and X. S. Xie, "Three-dimensional vibrational imaging by coherent anti-Stokes Raman scattering," *Phys. Rev. Lett.* **82**(20), 4142–4145 (1999).
22. C. L. Evans, E. O. Potma, M. Puoris'haag, *et al.*, "Chemical imaging of tissue in vivo with video-rate coherent anti-Stokes Raman scattering microscopy," *Proc. Natl. Acad. Sci.* **102**(46), 16807–16812 (2005).
23. M. Müller and A. Zumbusch, "Coherent anti-Stokes Raman Scattering Microscopy," *ChemPhysChem* **8**(15), 2156–2170 (2007).
24. C. Jüngst, M. J. Winterhalder, and A. Zumbusch, "Fast and long term lipid droplet tracking with CARS microscopy," *J. Biophotonics* **4**(6), 435–441 (2011).
25. P. Calzavara-Pinton, C. Longo, M. Venturini, *et al.*, "Reflectance confocal microscopy for in vivo skin imaging," *Photochem. Photobiol.* **84**(6), 1421–1430 (2008).
26. P. Guitera, G. Pellacani, K. A. Crotty, *et al.*, "The impact of in vivo reflectance confocal microscopy on the diagnostic accuracy of lentigo maligna and equivocal pigmented and nonpigmented macules of the face," *J. Invest. Dermatol.* **130**(8), 2080–2091 (2010).
27. C. Longo, I. Zalaudek, G. Argenziano, *et al.*, "New directions in dermatopathology In vivo confocal microscopy in clinical practice," *Dermatol. Clin.* **30**(4), 799–814 (2012).
28. Y. D. Xiong, S. Ma, X. Li, *et al.*, "A meta-analysis of reflectance confocal microscopy for the diagnosis of malignant skin tumours," *J. Eur. Acad. Dermatol. Venereol.* **30**(8), 1295–1302 (2016).
29. A. Levine and O. Markowitz, "Introduction to reflectance confocal microscopy and its use in clinical practice," *JAAD Case Reports* **4**(10), 1014–1023 (2018).
30. J. Lan, J. Wen, S. Cao, *et al.*, "The diagnostic accuracy of dermoscopy and reflectance confocal microscopy for amelanotic/hypomelanotic melanoma: a systematic review and meta-analysis," *Br. J. Dermatol.* **183**(2), 210–219 (2020).
31. C. Pezzini, S. Kaleci, J. Chester, *et al.*, "Reflectance confocal microscopy diagnostic accuracy for malignant melanoma in different clinical settings: systematic review and meta-analysis," *J. Eur. Acad. Dermatol. Venereol.* **34**(10), 2268–2279 (2020).
32. A. Scope, F. Farnetani, S. Haupt, *et al.*, "Dermoscopic and clinical predictors of reflectance confocal microscopy patterns of typical nevi on the back and legs: a cross-sectional study," *J. Am. Acad. Dermatol.* **85**(5), 1240–1247 (2021).
33. S. Kumar, T. Kamali, J. M. Levitte, *et al.*, "Single-pulse CARS based multimodal nonlinear optical microscope for bioimaging," *Opt. Express* **23**(10), 13082–13098 (2015).